Ferrite Number Prediction to 100 FN in Stainless Steel Weld Metal

A new constitution diagram has been developed that surpasses the Schaeffler and DeLong diagrams in accuracy

BY T. A. SIEWERT, C. N. McCOWAN AND D. L. OLSON

ABSTRACT. To improve the accuracy of ferrite number (FN) prediction in stainless steel weld metal, a new diagram has been developed using a database containing more than 950 alloy compositions from worldwide sources. In accuracy, this diagram surpasses the DeLong diagram for the low-FN austenitic stainless steel compositions of the 300 series, and it corrects a 2 FN bias detected for Type 309 stainless steel. The diagram is more accurate than the Schaeffler diagram for duplex stainless steel alloys and ferrite contents to 100 FN. It is most accurate when the Mn content is restricted to 10 wt-%, Mo content is restricted to 3 wt-%, N content is restricted to 0.2 wt-%, and Si content is restricted to 1 wt-%. Changes in the primary solidification mode are indicated on the diagram, and they appear to affect the FN response. Transitions in iso-FN line spacings may be caused by these mode changes.

Introduction

In many applications, the ability to control the delta-ferrite content of stainless steel weld metal is important. For example, the ferrite number (FN) is often used as an indicator of the resistance to fissuring (hot tearing) that occurs in many of the 300-series stainless steels (Ref. 1). Fissuring decreases rapidly over a small range (0–5 FN) of ferrite contents in these primarily austenitic phase weld compositions, so an accurate predictor of the FN is necessary to ensure the minimum ferrite levels that will prevent cracking. Fissuring should not be avoided by simply using materials with high FN values, since higher FN levels contribute to other undesirable behavior, such as an increased corrosion rate in certain environments (Ref. 2). Thus, there is incentive for keeping the FN in a limited range and for controlling the ferrite accurately.

At cryogenic temperatures, ferrite reduces the Charpy V-notch absorbed energy and the fracture toughness of the 300-series stainless steels (Refs. 3–6). The response is as dependent on ferrite content as is fissuring, but it reacts in the opposite direction. To provide the appropriate balance of cracking resistance and fracture toughness, the ferrite content must be controlled in a narrow range. Cryogenic applications require the most stringent FN controls and justify a search for more accurate FN prediction.

These examples have all been in the 0 to 25 FN range. In the past ten years, we have seen the development of new duplex stainless steel compositions for service conditions under which the austenitic grades are unsuitable. These alloys contain substantial amounts of both the austenite and ferrite phases, with the ferrite content being as high as 100 FN (roughly equivalent to 65 vol-% ferrite). For these alloys, Kotecki has recently shown relationships between the ferrite content and various mechanical properties, such as tensile strength and elongation (Ref. 7). So, in the high-FN range, it is important to control the ferrite content to achieve optimal weld properties. Unfortunately, few predictive diagrams have been developed for these compositions, and the data with which they were developed may not be accurate for today's compositions.

KEY WORDS

Ferrite Number (FN)
Stainless Steel Weld
Prediction to 100 FN
Duplex Stainless Steel
DeLong Diagram
Schaeffler Diagram
New Ni_{eq}/Cr_{eq} Diagram
Solidification Modes
Constitution Diagram

In the United States, the DeLong (Ref. 8) and Schaeffler (Ref. 9) diagrams are probably the most common methods for predicting the ferrite content of stainless steel weld metal. For both diagrams, a position on the diagram is determined from the composition and then related to a series of iso-ferrite or iso-FN lines. Both diagrams list the elements promoting the austenite phase along the vertical axis (as a term called Ni_{eq}) and the elements promoting the ferrite phase along the horizontal axis (as a term called Cr_{eq}). This nomenclature is based on naming the term after its primary component (Ni or Cr) and adding the other components, with appropriate coefficients to represent their relative power in promoting austenite or ferrite, to form an equivalent (Ni_{eq} or Cr_{eq}). The Schaeffler diagram (Fig. 1) uses straight lines that pivot around a common focus to represent the amount of ferrite as vol.-% over the range 0 to 100% (Ref. 9). The most recent version of the DeLong diagram (Fig. 2) uses nearly parallel lines to represent the amount of ferrite as FN over a narrower range of 0 to 18 FN (Ref. 8).

Earlier versions of the DeLong diagram represented ferrite in units of vol.-% only. The recent version was produced after the Welding Research Council (WRC) Subcommittee on the Welding of Stainless Steels promulgated a standard using the term ferrite number to define the ferrite content by its magnetic response. As a result, the DeLong diagram now contains both the FN and vol.-% ferrite designations, and it indicates that the two measurement systems begin to diverge at ferrite contents near 8 FN.

The two diagrams differ only slightly in their representation of compositional effects on ferrite content. The Cr_{eq} expressions are identical in the two diagrams—even the coefficients are the same. The DeLong Ni_{eq} expression contains all the elements and coefficients of the Schaeffler diagram but adds a term to include the effect of nitrogen on FN.

T. A. SIEWERT and C. N. McCOWAN are with the National Institute of Standards and Technology, Boulder, Colo. D. L. OLSON is with the Colorado School of Mines, Golden, Colo.

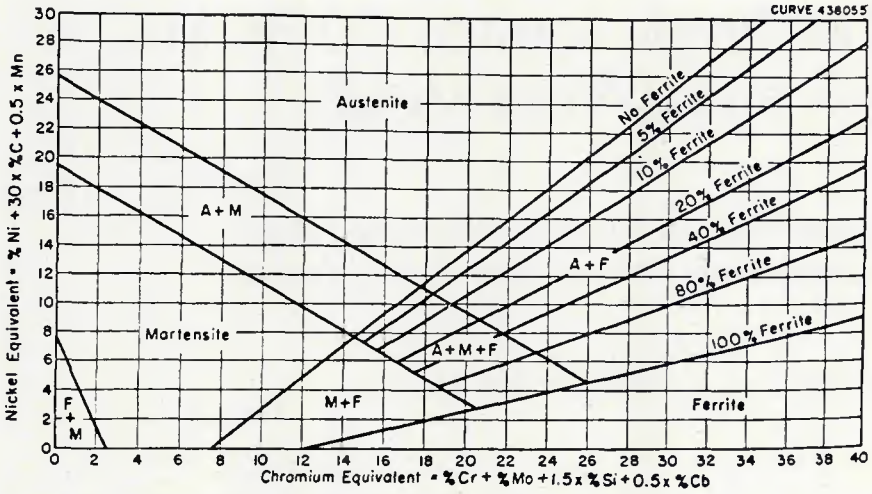

Fig. 1 — The Schaeffler constitution diagram for stainless steel weld metal

The difference in the applicability of the two diagrams is substantial. The DeLong diagram is a finely tuned subset of the Schaeffler range, designed specifically for the 300-series stainless steel welds containing small amounts of ferrite. Its widely accepted use with these alloys is documented by its inclusion in the AWS filler metal Specifications A5.4 and A5.9, and in the American Society of Mechanical Engineers (ASME) Boiler and Pressure Vessel Code. Prediction of FN for the compositions, such as the duplex stainless steels, that fall outside the range of the DeLong diagram seems to be the most common quantitative use of the Schaeffler diagram; however, its extension to fully ferritic compositions and the inclusion of martensitic regions provides much qualitative information about the general effect of alloying elements and the characteristic mechanical properties of alloy families.

Inaccuracies in both the DeLong and Schaeffler diagrams have become evident with the generation of new alloys and data. As a result, revisions of these diagrams have been proposed and several alternate diagrams have been developed (Ref. 10). The 0.5 coefficient for Mn is questioned by a number of researchers. Hull proposed a quadratic form indicating that Mn promoted austenite less as its content was increased, and actually promoted ferrite at very high levels (Ref. 11). Espy, in a study of stainless steels with up to 12.5 wt-% Mn and 0.31 wt-% N, concluded that Mn should not have a coefficient — its austenitizing potential could be better represented as a constant (Ref. 12). In a study of 41 specially formulated shielded metal arc electrodes with Mn levels gradually increasing to 13 wt-%, Szumachowski and Kotecki (Ref. 13) also determined that the Mn austenitizing potential could be represented as a constant, but suggested a value slightly smaller than Espy's. From a matrix of 26 electrodes containing up to 10 wt-% Mn and 0.26 wt-% N, McCowan and coworkers concluded that Mn and N interacted in a complex manner that could be expressed best by $Ni_{eq} = Ni + 29(C + N) + 0.53(Mn) - 0.05(Mn)^2 - 2.37(MnN) + 0.94(MnN)^2 - 0.71$ (Ref. 14). However, they also indicated that the effect of Mn could be adequately represented by a constant if a slightly poorer accuracy was accepted.

Other studies attempted to understand the effect of N. Espy reported a variable N coefficient, decreasing in value from 30 to 20 as the nitrogen content increases from 0.2 to 0.35 wt-% (Ref. 12). Others reported single-valued coefficients, ranging from 14.2 to 20 (Refs. 11,15–18). Ogawa and Koseki reported a coefficient of 30 for FN but a coefficient of 18 for the effect of N on solidification mode (Ref. 17).

Recently, Kotecki investigated the Si coefficient (Ref. 19). He found that the coefficient of 1.5, indicated by both the DeLong and Schaeffler diagrams, overstates the effect. In a study of six welds spanning 0.34 to 1.38 wt-% Si, he determined a coefficient of 0.1, which was significant for a 68% confidence interval. Another recent study found the silicon effect to be nonlinear and very small, below 2 wt-% Si, but large at higher silicon contents (Ref. 20).

Taken as a whole, these studies indicate that revisions of the DeLong and Schaeffler diagrams can substantially improve the accuracy of ferrite prediction for current stainless steel weld metal compositions.

Recent studies have emphasized that the solidification mode is more accurate than the FN for predicting the resistance to hot cracking (Refs. 21–23). These studies emphasize that the initial solidification structure (primary austenite or ferrite) directly determines the sensitivity to cracking by controlling the solubility of elements that promote cracking at these temperatures. These three studies contain data on both FN and primary solidification mode. These data were incorporated into the database for this study, which permitted comparison of the two types of data.

The goals of this study were 1) to develop a database containing recent FN data and new compositions, 2) to evaluate the DeLong and Schaeffler diagrams with these data, 3) to determine which elements were not being fit properly, and 4) to develop an improved predictive diagram that was continuous over the range 0 to 100 FN (roughly equivalent to 65 vol.-% ferrite). Ideally, this diagram would predict the ferrite content of the conventional 300-series stainless steels with at least the same accuracy as the

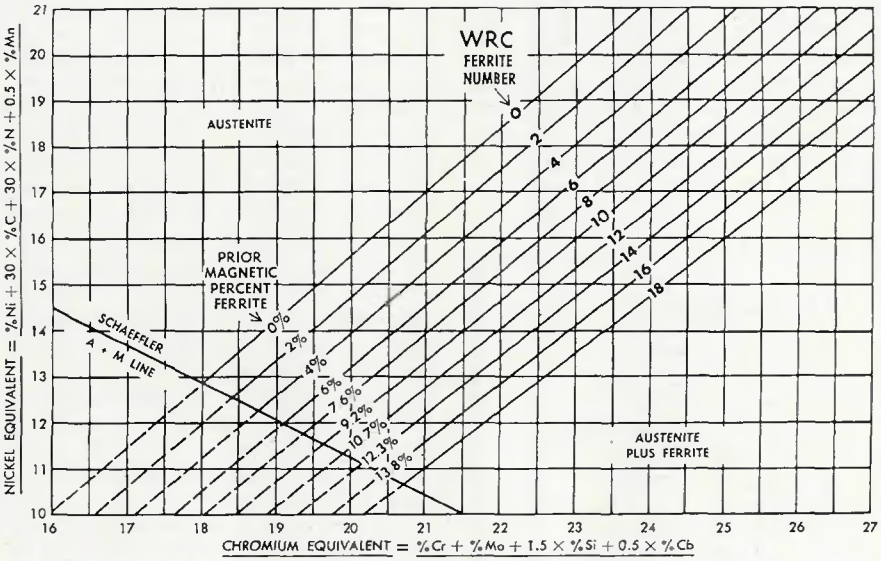

Fig. 2 — The DeLong constitution diagram, revised January 1973 to convert it to the Welding Research Council's ferrite number system for weld metals

DeLong diagram, duplex stainless steels with at least the same accuracy as the Schaeffler diagram, and be suitable for new alloys containing extended compositional ranges. It would also include primary solidification-mode data on the predictive diagram to reveal relationships to the FN response.

Database Development

The approach to the development of the database was 1) to gather a large sample of data for each of the common weld metal compositions that are now predictable by the DeLong diagram to ensure that these alloys would be predicted accurately by the new diagram, and 2) to include data of many special alloys to determine the limits of applicability and interactions.

Most of the data were obtained from members of the WRC Subcommittee on Welding of Stainless Steel. The nine sources of data included electrode manufacturers and research institutes, as well as some data from archival journals. The data well represented the common 300-series stainless steel weld compositions, Types 308, 308L, 309, 309L, 316 and 316L compositions. These data provided a good basis for evaluating the accuracy of the diagram and comparing scatter within and among the various sources. Other data represented duplex stainless steel compositions, experimental compositions designed to evaluate extended ranges for certain elements, and other new alloys. These data were used to determine element interactions and whether the behavior in the duplex range was a smooth extension of the behavior in the low-FN range.

From the data sources, we requested an FN measurement by the procedure specified in AWS A4.2 (Ref. 24) or by the procedure developed by Kotecki (Ref. 25) for extending the FN range to duplex alloys. The small fraction (approximately 1%) of the data for high-ferrite content alloys that was in vol.-% was converted to FN using Kotecki's procedure (Ref. 25). Matching each FN determination, we requested a complete chemical analysis specifically including C, Mn, Si, Cr, Ni, Mo, Ti, Nb and N. These data have been listed in the appendix to another report (Ref. 26). The compositional ranges in this database are summarized by element in Table 1.

Most of the data were received from manufacturers of welding electrodes, who had developed these data to certify that their products met a customer's requirements. Since specifications controlled the analysis and measurement techniques and these specifications contained limits for the critical parameters, the resulting data were quite consistent. This precluded the variation in the FN of a given composition that David, *et al.*, observed as the cooling rate was varied over several orders of magnitude (Ref. 27). In fact, the great majority of data were produced with shielded metal arc electrodes conforming to AWS Specification A5.4. Such uniformity in the electrodes, welding process, welding procedure and measurement reduces variations in FN due to these variables and permits a better fit of the data. The predictive equation does not consider these variables, because only composition and FN values were provided. The equation was not evaluated for welds produced under conditions outside those specified in A5.4.

Although the procedure developed by Kotecki for measurement of FN (Ref. 24) can be applied to fully ferritic alloys, they are outside the scope of this study. This study was limited to about 100 FN since few data were available above this level (almost none were supplied for the database), and at present there does not seem to be a need to predict above 100 FN.

Some of the data included primary solidification mode information following the nomenclature of Suutala (Ref. 21) (austenitic, austenitic-ferritic, ferritic-austenitic and ferritic). These were projected on the FN predictive diagram for comparison of mode changes with iso-FN lines.

To evaluate the existing diagrams in the most careful manner and to identify the sources of errors in prediction, the database was divided into groups, ten of which are listed in Table 2.

By comparing the quality of the fit of these groups with the fit of the entire database, we were able to determine the compositional range over which the elements could vary without degrading the accuracy of the predictive diagram. Similarly, these groups could be used to compare the effect of the various elements in the new and old diagrams.

Table 1—Compositional Range for Various Elements in the Database

Element	Range (wt-%)
C	0.01–0.15
Mn	0.4–12
Si	0.1–1.3
Cr	15–32
Ni	5–25
Mo	0–7
N	0.03–0.3
Nb	0–0.9
Ti	0–0.1

Table 2—Division of Database into Groups

Group	Description	Cases
1	Types 308 and 308L	220
2	Types 309 and 309L	129
3	Types 316 and 316L	139
4	FN < 18	796
5	FN < 18, and Mo < 3 wt-%	724
6	FN < 18, N < 0.1 wt-%, and Mo < 3 wt-%	652
7	FN < 18, N < 0.1 wt-%, and Mn < 3 wt-%	662
8	FN < 18, N < 0.1 wt-%, Mn < 3 wt-%, and Mo < 3 wt-%	605
9	FN < 30, Nb > 0	443
10	FN > 18	126

Procedure

A variety of statistical representations were used to evaluate the existing diagrams and the new expressions. To evaluate the existing diagrams, relative-frequency histograms were used. The measured FN was subtracted from the FN predicted by the diagram, and the difference (ΔFN) was plotted versus the error class intervals (different levels of error). A perfect fit would have resulted in a delta function centered at zero. The width of the distributions of the actual data around zero provided a measure of the variability, whereas an off-center peak revealed a bias.

The development of a new diagram began with a multiple linear regression, with FN as the dependent variable and the various elements that affect the FN as independent variables. The process has been described previously (Ref. 6). Briefly, it consists of the selection of the variable (alloying element) that most strongly determines the FN and production of a linear predictive equation. The program then chooses the next most influential variable and develops a new equation. The process is repeated in a stepwise manner until the addition (or subtraction) of further terms will not statistically improve the prediction of FN. The coefficients for the various elements in these equations were compared with the coefficients in the existing diagrams. After evaluating the various groups of data individually, differences in their coefficients could be used to determine which elements and compositions were the dominant sources of scatter in the overall predictive diagram.

Next, the coefficient of each element was checked for accuracy. Our approach was similar to a technique reported by Szumachowski and Kotecki (Ref. 13). To evaluate the various coefficients that have been suggested for Mn, they developed a term, ΔNi_{eq}, by subtracting from the measured FN value the contributions of all other elements and plotting this term versus the concentration of Mn.

This term, ΔNi_{eq}, was effectively the combination of the response of the FN to one particular element (Mn) confounded with the random error in the data. When they were unable to resolve a slope for the data, they concluded that Mn had no effect.

Our stepwise linear regression program produced a file of the residuals (error left after the fitting program was finished) for the data. We plotted this versus the various elements that had not met the selection criteria of the regression program. For the elements that had been selected by the regression program, we added the residuals to the product of the element concentration and the selected coefficient. We called this term ΔNi_{eq} (or ΔCr_{eq} if the element functioned as a ferritizer) since it contains the same information as the term used by Szumachowski and Kotecki (Ref. 13), even though it was generated in a slightly different manner. The slope of the best-fit line through the ΔNi_{eq} or ΔCr_{eq} versus element concentration data was the coefficient for the element. This technique allowed us to evaluate the quality of the fit and to search for nonlinear behavior. By allowing various ranges of other elements, we also searched for element interaction effects.

When we had incorporated the changes indicated by this technique into our predictive equation, we used the equation to produce a FN map. The map began as a blank FN diagram; its axes consisted of the Ni_{eq} and Cr_{eq} from our best linear equation. The computer calculated a position for each datum, from the Ni_{eq} and Cr_{eq} expressions, and identified that point by the measured FN. The program created a map by linear interpolation between measured FN values and then generated iso-FN contour lines to represent the data. This technique enabled us to separate the nonlinear response of the individual elements over the entire range of the diagram from the nonlinear response in a specific region of the diagram (*i.e.,* to improve the fit by using either nonlinear coefficients or curved and unevenly spaced iso-FN lines). The difference, ΔFN, between measured and predicted FN, was also computed.

As a final check on the accuracy of the diagram, the ΔFN values from the mapping program were plotted versus the element concentrations, as was done after the linear fit by using the procedure for the ΔNi_{eq} and ΔCr_{eq}. By comparing these plots to the ΔNi_{eq} and ΔCr_{eq} plots, we could assure ourselves that the mapping procedure produced a diagram that was at least of the same quality as the linear equation and determine whether any nonlinear behavior could now be resolved.

The solidification-mode data were also plotted on the map to relate the solidification mode to the FN behavior.

Results and Discussion

Construction of a New Diagram

To determine more accurate representations of the FN potential for the Type 308, Type 309 and Type 316 alloys, the multiple linear regression technique was applied to each data group. Three predictive equations were generated.

For 308-type alloys,

$$FN = -27 + 3(Cr + 0.8Mo) - 1.9(Ni + 49C + 29N); \quad (1)$$

for 316-type alloys,

$$FN = -13 + 2.2(Cr + 2.3Mo) - 2(Ni + 40C + 24N); \text{ and} \quad (2)$$

for 309-type alloys,

$$FN = -31 + 3.2(Cr + 1.1Mo) - 2(Ni + 53C + 17N). \quad (3)$$

The R^2 values (a statistical measure of the fit that approaches 1 with better fits) for these three equations were 0.74, 0.89 and 0.77; the standard deviations of the residuals were 1.3, 1.1 and 1.3 FN, respectively. The Cr_{eq} and Ni_{eq} terms are the quantities in parentheses with the various elements in units of wt-%. The differences in the coefficients for the elements and the Cr_{eq} and Ni_{eq} terms are due to differences in the behavior within the alloy range, as well as to difficulties in fitting a line to data that are in a small cluster. Because of inaccuracies due to data clusters, these equations are not recommended for general use, but the equations do point out that each alloy range generates a characteristic set of coefficients.

The differences in the equations also emphasize that an empirically developed predictive diagram developed for many alloys can only approximate the behavior of a specific alloy group. Until we can develop a model that truly represents the physical phenomena of the ferrite transformations, we must use a variety of fitting constants and statistical techniques to develop a diagram that provides predictions of acceptable accuracy. Although the optimum coefficients for each alloy group are different, the general equation forms are quite similar. This suggests that a single equation with compromise values for the coefficients might be able to predict the FN with an acceptable degree of accuracy.

Next, we processed the data of Group 8 (FN < 18, N < 0.1 wt-%, Mn < 3 wt-%, and Mo < 3 wt-%) through the multiple linear regression program. The Group 8 data cover a broad range of compositions and produced equivalents with a range of applicability equal to that of the DeLong diagram. From Group 8, we excluded the data for FN < 1 and the AF solidification mode, since we anticipated nonlinearities due to ferrite formed mechanically during surface preparation and in differing solidification modes. The predictive equation for Group 8 alloys and alloys with FN > 1, and solidifying in the FA mode is

$$FN = -18 + 2.9(Cr + Mo + 0.3Si) - 2.6(Ni + 35C + 20N + 0.3Mn) \quad (4)$$

is analogous to the DeLong diagram. For this equation, R^2 is 0.78 and the standard deviation of the residual is 1.6 FN. These parameters are similar to those for the alloy groups considered above and confirm that one equation can provide a fairly accurate prediction over a range of compositions. This equation has coefficients similar to Equations 1 through 3; in fact, it is almost the average of the behavior for the three alloy groups. In Equation 4, the coefficients of C and N within the parentheses are smaller, but when multiplied by the coefficient outside Ni_{eq} parentheses, the values are close to those of Equations 1 through 3. The main difference is the larger effective coefficient for Ni, 2.6, as compared to 1.9 or 2. Equations 1 through 4 all indicate that the effect of C is greater than that of N, unlike the equal effects predicted by DeLong. The C/N coefficient ratios are 1.7, 1.6, 3.1 and 1.8 for these equations, respectively. Similar C/N coefficient ratios have been found in other FN studies and a ratio of 1.5 is used in the Hammar solidification equivalents (Refs. 10, 12, 14, 15).

Equation 4 is the best fit for a linear regression model, that is, an arithmetic combination of linear terms producing a diagram with equispaced and parallel lines. The following subsections investigate the possibility of improving the prediction when these requirements are relaxed.

ΔNi_{eq} and ΔCr_{eq}

Compositional terms defined by the best-fit linear equation (Equation 4) were evaluated using ΔNi_{eq} and ΔCr_{eq} plots described in the procedure. Although the technique was intended primarily to find second-order or other nonlinear behavior, it also confirmed that the coefficient determined during the linear regression program was the best line through the data. We did note the existence of some interactions. Comparison of ΔCr_{eq} for Cr and Mo plots for the Group 4 data revealed that Cr could be given a coefficient of 1 and possess little scatter when the Mo content was less than 3 wt-%. For higher Mo contents, the behavior was substantially different, with a level of scatter that precluded determination of a mathematical representation.

We were unable to confirm the nonlinear trends reported for Mn (Ref. 11) or Mn-N (Ref. 14), but unless these trends were of substantial magnitude, their effects would have been hidden by the scatter in the data collected from many

sources. The ΔNi_{eq}-Mn plots did indicate that scatter about the 0.3 slope expressed for Mn in Equation 4 dependent on Mn and N contents. The effect is relatively small (about 3 FN at 10 wt-% Mn), however, and not statistically significant at an F level of 4 (a statistical measure of fit roughly corresponding to a 95% confidence level). In addition, manganese was often chosen as a ferrite stabilizer when the duplex stainless steel data (Group 10) was evaluated. Thus, a Mn term is not included in the Ni_{eq}.

Since the DeLong and Schaeffler diagrams include coefficients for Si and Nb, the ΔCr_{eq} plots for these elements were of particular interest. When welds having reported Nb contents were used (Group 9), the plot revealed a slope corresponding to a coefficient near 0.7. The absence of the 0.7-Nb term causes a 2 FN bias for a Type 347 composition, so the term should be added to the Cr_{eq} to adjust for the Nb effect.

When the ΔCr_{eq} is examined for a Si effect, a slight trend is also evident. For Equation 4, a coefficient of 0.3 was determined for Si, but as was the case for Mn, the statistical significance of the Si term was low. When this coefficient is multiplied by the expected range in Si content and converted to ΔFN, the value is near 1 FN. The small statistical significance of this value combined with the limited range in Si contents, caused us to exclude it from the predictive diagram.

The ΔCr_{eq} plot for Ti was also examined for a coefficient or interaction with N or C. No clear relationships could be resolved.

Although no nonlinear terms could be resolved and used to refine the Ni and Cr equivalents in the FN equation, the levels where the scatter increased (3 wt-% for Mo, 3 wt-% for Mn and 0.1 wt-% for N) were used to evaluate the FN diagram.

Mapping

After confirming that they could not be improved by the use of nonlinear or interactive terms, the Ni and Cr equivalents were used with a mapping program that relaxed the restriction of parallel and equispaced lines. The resulting diagram using the entire database is shown in Fig. 3. Straight lines fit well in the Ni_{eq} range of 9 to 17, and in the Cr_{eq} range of 17 to 30. Above a Ni_{eq} of 17, there was some evidence of curvature (dotted lines), but a scarcity of data prevented deduction of the true behavior. The appearance is very similar to that of the Schaeffler diagram in Fig. 1.

Another feature of the DeLong and Schaeffler diagrams is a line denoting martensite formation in the lower left region of the diagrams. This line provides valuable guidance on compositions where this magnetic phase might exist,

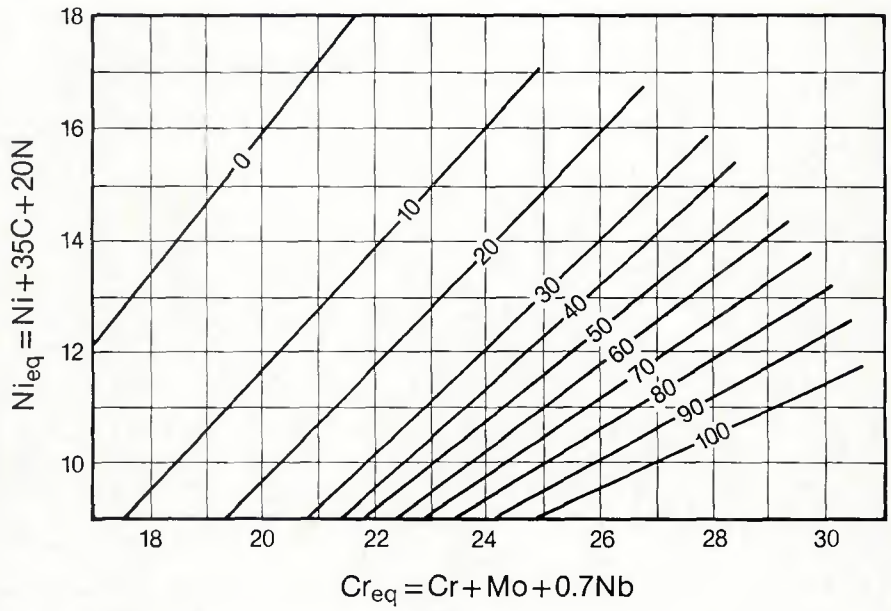

Fig. 3—New diagram produced by mapping program

the presence of which would add to the apparent value of FN. This line cannot be directly transferred to the new diagram, because the Cr_{eq} and Ni_{eq} are defined differently. A recent study of martensite formation indicated martensite would not be expected over the range of compositions and indicated coefficients far different than those of the new diagram (Ref. 28). Therefore, a line denoting the region where martensite and austenite could coexist was not included. Examination of the lower-left region of the map does not reveal a change in line slope and so the effect of martensite seems small for the commercially useful data we studied.

The diagram contains equispaced parallel lines between FN values of 4 and 12, explaining the success of the DeLong diagram in the 0- to 18-FN range with nearly parallel lines. The rapid compression of line spacing above a FN of 12 and the rotation of the lines above a FN of 35 explains why the DeLong diagram could not be extended to duplex compositions. The compression of line spacings and rotation at these higher FN lines explains why the Schaeffler diagram has provided the best estimate of FN in this region. To determine whether the new diagram represents the FN more accurately than the Schaeffler or DeLong diagrams, quantitative comparisons were made.

Evaluation of the New Diagram

The new diagram should have been evaluated using an independent database. However, all available data were used in the development of the new diagram. Since the data were gathered from many sources and are assumed to represent current alloy production, they were used to compare the accuracy of the new diagram to the DeLong and Schaeffler diagrams. Because these older diagrams have distinctly different ranges, they are considered separately.

Comparison to the DeLong Diagram (0–18 FN)

Since the DeLong diagram was developed for use with the conventional 300-series stainless steel compositions, the measured FN values of the Type-308, -309, and -316 data groups were compared with those predicted by the DeLong diagram. Relative-frequency histograms of the error distributions are included as Figs. 4 through 6. Since each of the groups contains the data for over 100 welds collected from many sources, they are considered to be representative of current alloy production. The Type-308 and -316 data (Figs. 4 and 6) exhibit the expected Gaussian error distribution centered on zero with a standard deviation near 2 FN. The Type-309 data (Fig. 5) exhibit a similar distribution shape and standard deviation, but they are centered near −2 FN. Such a bias in the mean indicates that predictions based on the diagram are inaccurate for these Type-309 compositions and do not meet the ±3 FN accuracy reported for 90% of the data during the development of the DeLong diagram (Ref. 8). Separation of the data by source confirmed the same bias for each. Only 43% of the Type-309 data was predicted within a ±2.5 FN error. For the Type-308 and -316 data groups, 82 and 91% of the welds were predicted within a ±2.5 FN error, respectively. In comparison, the new diagram predicted 88% of the Type-308, 91% of the Type-316, and 92% of the Type-309 data within a ±2.5 FN error. So, the new diagram is more accurate, especially for the Type-309 compositions.

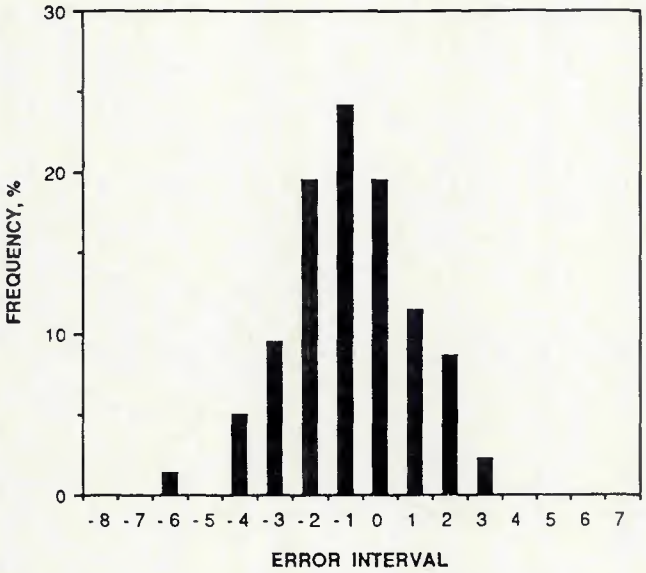

Fig. 4 — Relative-frequency histogram of the error distribution for the Type-308 data as evaluated by the DeLong diagram

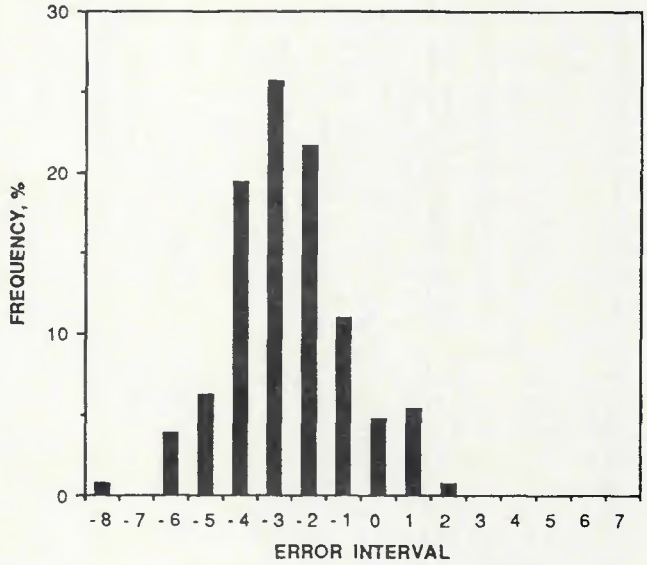

Fig. 5 — Relative-frequency histogram of the error distribution for the Type-309 data as evaluated by the DeLong diagram

For a broader, more comprehensive evaluation, all the data that had an FN less than 18 (data Group 4) was evaluated. Both the DeLong diagram and the new diagram were used to compute the FN for these compositions. Again, relative-frequency histograms were used to search for bias or a non-Gaussian shape in the error distribution. The histogram shapes were normal; no bias was found. For all the data with an FN less than 18, the DeLong diagram predicted 66% with an error less than 2.5 FN, whereas the new diagram predicted 84%.

Although the comparisons made between the relative errors found for DeLong and the new diagram are useful, error magnitudes determined for the DeLong diagram here should not be compared to the accuracy statement (90% of data within ±3 FN) in that report (Ref. 8). The DeLong diagram was developed and evaluated on data from a single laboratory using procedures more stringent than those in AWS A4.2. This database contains additional error due to interlaboratory dissimilarities in welding procedures and specimen preparation techniques. Another complication in the evaluation is that some of the data were outside the Cr_{eq} boundaries of the published DeLong diagram. Since we chose to evaluate the DeLong diagram only over its reported range, we excluded these data. Similarly, for the proposed diagram, computer mapping restrictions limited the Cr_{eq} range and excluded a small portion of the data. Manual evaluation of these data revealed that they fit the extension of the reported lines, but the scarcity of the data and difficulty of manual calculations caused us to limit the scope of the diagram to that reported. The number of cases considered for the two diagrams is included in Table 3.

Because this study and others (Refs. 12, 14) have shown the behavior of some elements to be interactive and, therefore, the cause of some scatter, the diagrams were evaluated using data Groups 5–8, which had several different combinations of compositional restrictions. Their evaluation is also summarized in Table 3.

The restriction of the Mo content to less than 3 wt-% resulted in a 2% improvement in the accuracy of the DeLong diagram, and a 4% improvement in the accuracy of the proposed diagram. This significant improvement in the proposed diagram may be the result of a Cr-Mo interaction that is excluded when Mo levels were limited to 3 wt-% during the ΔCr_{eq} analysis or incomplete dissolution of the high-melting-point Mo contained in the electrode coating.

Smaller improvements are noted as the N is restricted to less than 0.1 wt-% in Group 6 or the Mn is restricted to less than 3 wt-% in Groups 7 and 8. The best fit for both diagrams occurs for Group 8, when all four restrictions (similar to the reported range of applicability of the DeLong diagram) are invoked. However, the improvement over Group 5 is so slight for the proposed diagram that the Group 5 restrictions provide the best combination of accuracy and coefficient simplicity. Scarcity of data at very high element concentration levels does suggest some further restrictions; Mn < 10 wt-% and N < 0.2 wt-%. With these restrictions, the proposed diagram has better than an 88% chance of predicting the FN with an accuracy of ±2.5 FN, a value substantially better than the 68% chance for the DeLong diagram.

To confirm the validity of these restrictions and to search for nonlinear behav-

Fig. 6 — Relative frequency histogram of the error distribution for the Type-316 data as evaluated by the DeLong diagram

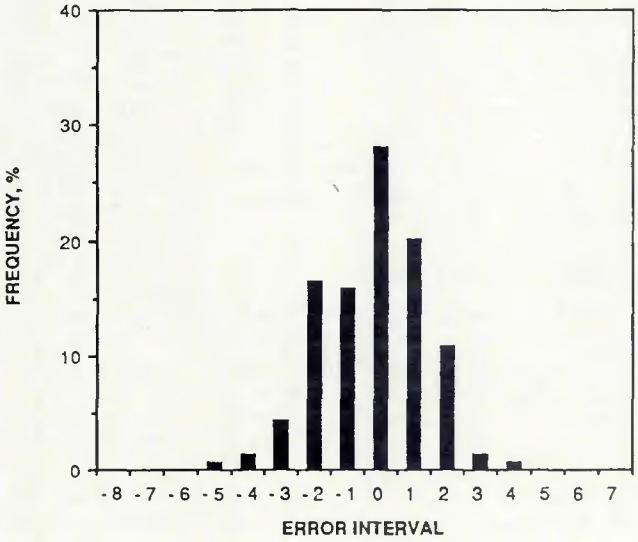

ior, the ΔFN for the proposed diagram was plotted versus the various elements. These plots more clearly show trends seen during ΔNi_{eq} and ΔCr_{eq} analyses.

The plot of ΔFN versus Cr content in Fig. 7 uses the Group 5 data and has a restricted carbon range that helped to reduce the scatter. The greater scatter with increasing Mo content is clearly visible. Both a Cr-Mo interaction or incomplete dissolution of Mo added to the weld pool by means of the electrode coating could explain this scatter. No reduction in scatter was apparent for Mo limits lower than 3 wt-%. This reinforces the value of restricting Mo content to 3 wt-% for increased prediction accuracy.

In the plot of ΔFN versus Mn content in Fig. 8, the Mo content is below 3 wt-%, the FN is below 30 and the Ni content is above 8 wt-%. The divergence in the Mn response is evident for the two levels of N at Mn levels above 6 wt-%. At high-Mn and -N contents, little error in predicted FN values from the new diagram would be expected. For high-Mn and low-N contents, however, Mn appears to have a slight ferrite stabilizing effect. The error is much smaller than that for the Cr-Mo interaction. A limit for the Mn of 10 wt-% is indicated by the scarcity of data above this value.

Comparison to the Schaeffler Diagram (0 to 100 FN)

The full range of ferrite content is covered by the Schaeffler diagram (Fig. 2), but this diagram is in vol.-% ferrite rather than FN. So the FN data were converted to vol.-% ferrite by the procedure of Kotecki (Ref. 25). Thus, we compared the error for the Schaeffler diagram (using this database converted to % ferrite) with the error for the proposed diagram (using this database in FN). However, comparison of these two relative-frequency histograms is difficult because they are in different units. To bring the error class intervals into agreement, we assumed that 1%-ferrite error is approximately equal to 1.5-FN error, a reasonable average for the range of the database. In this way, we produced comparable class interval widths to enable a more direct comparison of error in the two diagrams.

Since the addition of a N coefficient was one of the factors in the wide acceptance of the DeLong diagram, we also prepared a modified Schaeffler diagram containing N. Using DeLong's coefficient of 30, we fit the Schaeffler diagram to the entire database and obtained a 0.05 wt-% offset term. This meant that the N content should be reduced by 0.05 before being multiplied by 30 and added to the Ni_{eq}.

The proposed diagram and the Schaeffler diagram are compared in Table

Table 3—Comparison of the Accuracy of the DeLong Diagram and the Proposed Diagram for Various Data Groups

Data Group	Description[a]	Error Less Than ± 2.5 FN (%) DeLong	Error Less Than ± 2.5 FN (%) Proposed	Cases Used DeLong	Cases Used Proposed
4	FN < 18	66	84	747	723
5	FN < 18 and Mo < 3	68	88	706	660
6	FN < 18, Mo < 3, and N < 0.1	68	87	643	606
7	FN < 18, Mn < 3, and N < 0.1	69	85	635	622
8	FN < 18, Mn < 3, Mo < 3, and N < 0.1	71	89	601	573

(a) Element concentrations in wt-%.

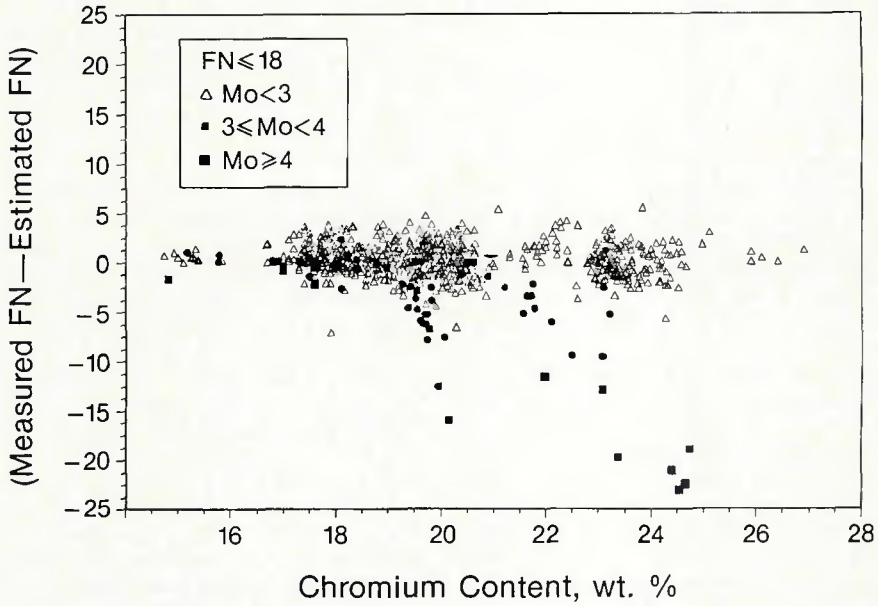

Fig. 7—Plot of FN versus chromium content for the new diagram indicating a Cr-Mo interaction

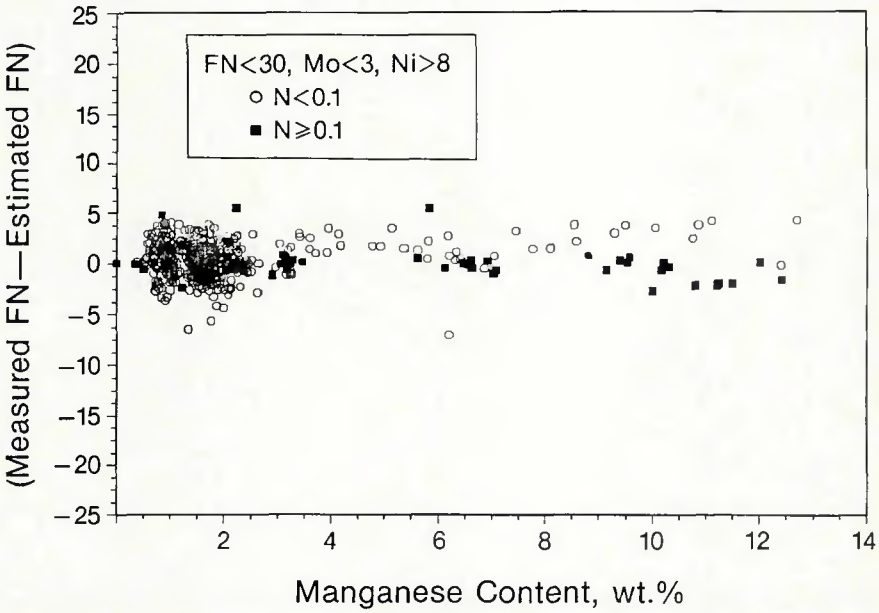

Fig. 8—Plot of FN versus manganese content for the new diagram indicating a Mn-N interaction

Table 4—Comparison of the Accuracy of the Schaeffler Diagram and the Proposed Diagram

Data Group Description	Error Less Than ± 9 FN (%)		Cases Used	
	Schaeffler	Proposed	Schaeffler	Proposed
FN > 18	35	70	124	125
FN < 18	52[a]	84[a]	771	740

(a) Error less than ± 2.5 FN.

4 for two FN ranges. For FN values greater than 18, the Schaeffler diagram is substantially less accurate than the proposed diagram. Examination of the error histograms revealed that the error for the new diagram had a Gaussian shape centered on zero, while that for the Schaeffler diagram was skewed but centered on zero.

For FN values less than 18, the Schaeffler diagram is substantially less accurate than the proposed diagram and somewhat less accurate than the DeLong diagram (Table 3). Again, the error histogram for the proposed diagram was Gaussian and centered on zero, while the error histograms for the Schaeffler diagram was centered on zero but skewed. The addition of the N term improved the accuracy of the (revised) Schaeffler prediction to 70% for FN < 18 (greater accuracy than the DeLong diagram); however, the error distribution for 309 data was heavily skewed, but it is still poor compared to the proposed diagram in this FN range. Comparison of the three error histograms (proposed, revised Schaeffler with the N term and DeLong diagrams) indicated the proposed diagram was characterized by a Gaussian shape centered on zero, while the revised Schaeffler diagram was characterized by a smaller skew to one side and the DeLong diagram was characterized by a distribution not centered on zero (biased). It appears that the DeLong diagram improved on the Schaeffler diagram by adding the N term and reducing the skewed distribution for FN < 18. The proposed diagram improves on the DeLong diagram by eliminating the bias and choosing new coefficients that narrow the standard deviation of the error histogram.

Solidification Mode

Hammar (Ref. 15) and Suutala (Ref. 21) evaluated and discussed the use of a predictive equation for the boundaries between the various solidification modes. Suutala's solidification data, along with data from Kujanpaa (Ref. 23) and Ogawa (Ref. 17) were used in this study to evaluate solidification-mode boundaries for the proposed FN diagram. When the solidification mode was plotted on our Ni_{eq} and Cr_{eq} coordinate axes, the separation between the modes was very distinct (Fig. 9), perhaps as good a separation as with the Hammar-Suutala coordinate axes (Fig. 10), which were designed specifically for solidification-mode separation. This result indicates that the high-temperature solidification behavior has a similar dependence on composition as does the amount of ferrite retained to room temperature (FN). Based on the good separation of the solidification modes with our Ni_{eq} and Cr_{eq} expressions, we believe it is premature to conclude that separate Ni_{eq} and Cr_{eq} expressions are necessary to predict FN and solidification mode in stainless steel welds. Therefore, the boundaries determined for the various solidification zones in Fig. 9 are included on the proposed predictive diagram—Fig. 11.

The location of the solidification-mode boundaries corresponds well to changes in the FN response. When solidification boundaries from the top of the diagram are considered, the A to AF (austenite to combined austenite-ferrite) solidification boundary falls directly on the zero-FN line, the transition between a fully austenitic and a partially ferritic structure.

The AF to FA (austenite-ferritic and ferritic-austenitic) boundary denotes the change to a primary ferritic structure, which has been related to a substantial reduction in hot-cracking sensitivity. Using the fissuring data given by Lundin (Ref. 1), we noticed that the reported FN needed to eliminate fissures corresponds very closely to the AF to FA boundary on the diagram. They reported minimum FN to prevent fissures of 1.5 for Type 316L (Cr_{eq} near 20), 2 for Type 308 Cr_{eq} near 18.5), 2.5 for Type 316 (Cr_{eq} near 20.5), 3 for Type 308L (Cr_{eq} near 18.8), and 4 for Type 309 (Cr_{eq} near 23). This suggests that the AF to FA boundary could be used as an accurate guide to controlling the hot-cracking tendency as Kujanpaa also noted in his study (Ref. 23).

The FA to F (ferrite-austenite to ferrite) transition corresponds to the beginning

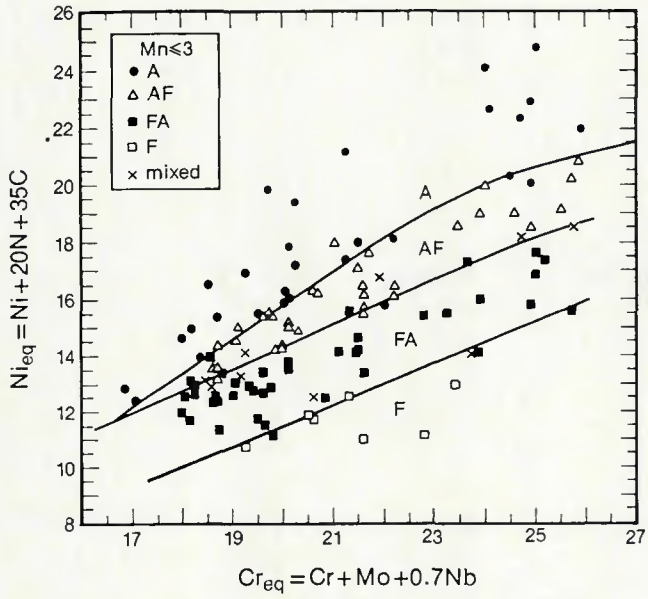

Fig. 9—Solidification mode date on the coordinate axes of the new diagram

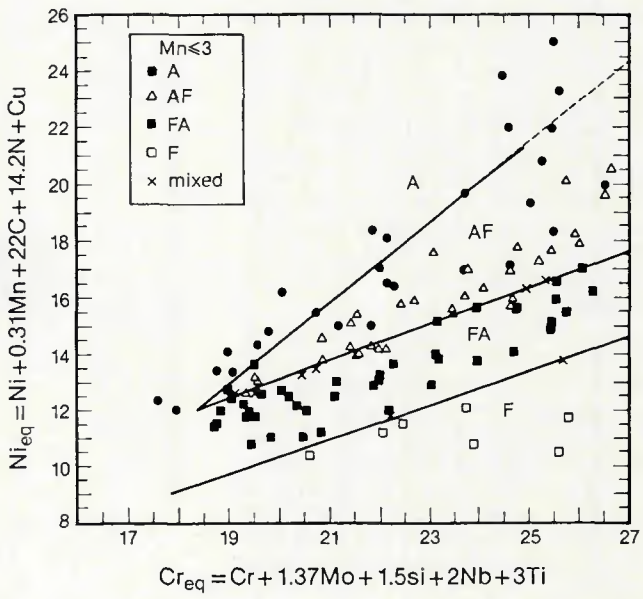

Fig. 10—Solidification mode data on the coordinate axes of Hammar and Svenson

of a compression in FN spacing, then the start of rotation of the lines. Microstructurally, this corresponds to a change from a vermicular to a lath structure as the austenitic phase is forced to nucleate within a ferritic phase.

The relationship between FN and solidification mode is shown from a slightly different perspective in Fig. 12. Here, the modified solidification equivalents of Suutala (Ref. 21) were used as coordinate axes when mapping the iso-FN lines. The FN lines are not as straight with these equivalents, and they do not model compositional effects over as broad a range as the proposed FN equivalents, but these equivalents indicate an interaction between FN and solidification mode. We noted a tendency for the iso-FN lines to move parallel to the boundary between AF and FA solidification zones and saw indications that iso-FN slopes may differ in these respective solidification zones.

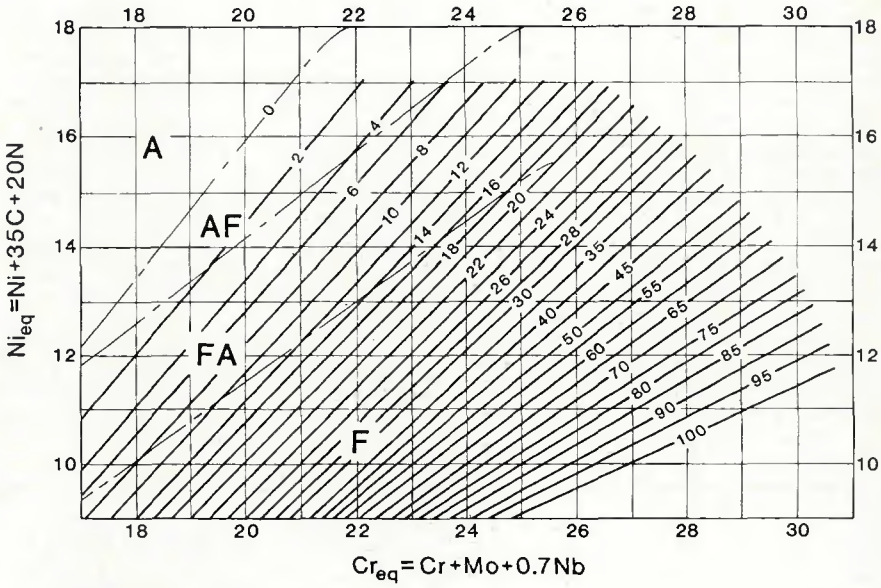

Fig. 11—New diagram, including solidification-mode boundaries

Conclusions

1) A new predictive diagram for ferrite in stainless steels has been developed for the range 0 to 100 FN.

2) The diagram is applicable for Mn contents to 10 wt-%, Mo contents to 3 wt-%, N contents to 0.2 wt-% and Si contents to 1 wt-%.

3. The accuracy of the diagram surpasses that of the DeLong and Schaeffler diagrams in this range for a 950-point database.

4) Diagram includes solidification boundaries that correspond to changes in FN response. AF to FA boundary seems to be a good predictor of cracking sensitivity.

Acknowledgments

The authors acknowledge financial support from the Department of Energy and the Welding Research Council. The authors are also indebted to Alloy Rods Co.; Teledyne McKay; Sandvik Steel Co., Welding and Wire Division; Smitweld; Soudometal and the Welding Institute, who supplied data. The authors also acknowledge helpful comments and reviews by W. T. DeLong, D. J. Kotecki, F. B. Lake, R. D. Thomas, Jr., and D. F. Vecchia, as well as guidance provided by J. E. Koontz and J. R. Donaldson on the use of statistical and graphics programs used in this study.

References

1. Lundin, C. D., DeLong, W. T., and Spond, D. F. 1975. Ferrite-fissuring relationship in austenitic stainless steel weld metals. *Welding Journal* 54(8):241-s to 246-s.

2. Baeslack, III, W.A., Duquette, D.J., and Savage, W.F. 1978. Technical note: stress corrosion cracking in duplex stainless steel weldments. *Welding Journal* 57(6):175-s to 177-s.

3. Siewert, T. A. 1978. How to predict impact energy from stainless steel composition. *WD&F* 51:88-90.

4. Szumachowski, E. R., and Reid, H. F. 1978. Cryogenic toughness of SMA austenitic stainless steel weld metals: part 1—role of ferrite. *Welding Journal* 57(11):325-s to 333-s.

5. Read, D. T., McHenry, H. I., Steinmeyer, P. A., and Thomas, Jr., R. D. 1980. Metallurgical factors affecting the toughness of 316L SMA weldments at cryogenic temperatures. *Welding Journal* 59(4):104-s to 113-s.

6. Siewert, T. A. 1986. Predicting the toughness of SMA austenitic stainless steel welds at 77 K. *Welding Journal* 65(3):23-28.

7. Kotecki, D. J. 1987. Ferrite control in duplex stainless steel weld metal. *Welding Journal* 65(10):273-s to 278-s.

8. DeLong, W. T. 1974. Ferrite in austenitic stainless steel weld metal. *Welding Journal* 53(7):273-s to 286-s.

9. Schaeffler, A. 1949. Constitution diagram for stainless steel weld metal. *Metal Progress* 56:680-680B.

10. Olson, D. L. 1985. Prediction of austenitic weld metal microstructure and properties. *Welding Journal* 64(10):281-s to 295-s.

11. Hull, F. C. 1973. Delta ferrite and martensite formation in stainless steels. *Welding Journal* 52(5):193-s to 203-s.

12. Espy, R. H. 1982. Weldability of nitrogen-strengthened stainless steels. *Welding Journal* 61(5):149-s to 156-s.

13. Szumachowski, E. R., and Kotecki, D. J. 1984. Effect of manganese on stainless steel weld metal ferrite. *Welding Journal* 63(5):156-s to 161-s.

14. McCowan, C. N., Siewert, T. A., Reed, R. P., and Lake, F. B. 1987. Manganese and nitrogen in stainless steel SMA welds for cryogenic service. *Welding Journal* 66(3):84-s to 92-s.

15. Hammar, O., and Svenson, U. 1979. *Solidification and Casting of Metals*. The Metals Society. London, England, pp. 401-410.

16. Mel'Kumor, N., and Topilin, V. V. 1969. Alloying austenitic stainless steel with nitrogen. *Obrabotka Metallor* (8):47-51.

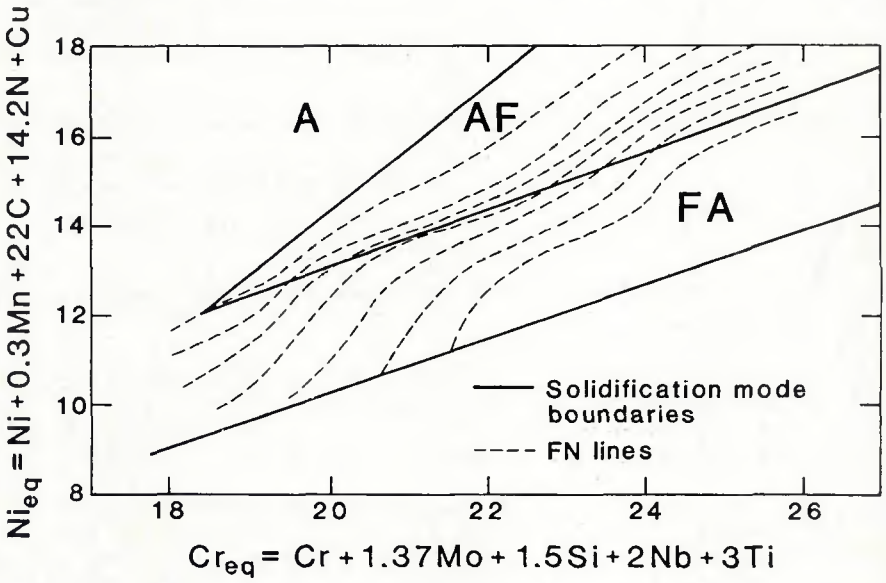

Fig. 12—Schematic representation of iso-FN line shape near solidification mode boundaries, indicating a coupling between the two

17. Ogawa, T. and Koseki, T. 1988. Weldability of newly developed austenitic alloys for cryogenic service: part II—high-nitrogen stainless steel weld metal. *Welding Journal* 67(1):8-s to 17-s.

18. Okagawa, R. K., Dixon, R. D., and Olson, D. L. 1983. The influence of nitrogen from welding on stainless steel weld metal microstructure. *Welding Journal* 62(8):204-s to 209-s.

19. Kotecki, D. J. 1986: Silicon effect on stainless weld metal ferrite. *IIW. Doc. II-C-779-86.* The American Council of the International Institute of Welding. Miami, Fla.

20. Takemoto, T., Murata, Y., and Tanaka, T. 1987. Effect of manganese on phase stability of Cr-Ni nonmagnetic stainless steel. In *High Manganese Austenitic Steels,* Ed. R.A. Lula, ASM Conference Proceeding, Oct. 10–15, 1987, ASM Intl., Cincinnati, Ohio. pp. 23–31.

21. Suutala, N. 1982. Effect of manganese and nitrogen on the solidification mode in austenitic stainless steel welds. *Met. Trans. A*

22. Lippold, J. C., and Savage, W. F. 1982. Solidification of austenitic stainless steel weldments: part III—the effect of solidification behavior on hot cracking susceptibility. *Welding Journal* 61(12):388-s to 396-s.

23. Kujanpaa, V. 1985. Role of steel type and impurities in solidification cracking in austenitic stainless steel welds. *Metal Construction* pp. 23–25.

24. *Standard Procedures for Calibrating Magnetic Instruments to Measure the Delta Ferrite Content of Austenitic Stainless Steel Weld Metal.* ANSI/AWS A 4.2-86, American Welding Society. Miami, Fla.

25. Kotecki, D. J. 1982. Extension of the WRC ferrite number system. *Welding Journal* 61(11):352-s to 361-s.

26. McCowan, C. N., Siewert, T. A., and Olson, D. L. 1989. Stainless Steel Welds: Prediction of Ferrite Content. Welding Research Council Bulletin, 343, May 1989.

27. David, S. A., Vitek, J. M., and Hebble, T. L. 1987. Effect of rapid solidification on stainless steel weld metal microstructures and its implications on the Schaeffler diagram. *Welding Journal* 66(10):289-s to 300-s.

28. Self, J. A. 1986. *Effects of Composition upon the Martensitic Transformation Temperature of Austenitic Stainless Steel Welds,* Thesis. Colorado School of Mines, University Microfilms, Ann Arbor, Mich.

WRC Bulletin 330
January 1988

This Bulletin contains two reports covering the properties of several constructional-steel weldments prepared with different welding procedures.

The Fracture Behavior of A588 Grade A and A572 Grade 50 Weldments
By C. V. Robino, R. Varughese, A. W. Pense and R. C. Dias

An experimental study was conducted on ASTM A588 Grade A and ASTM A572 Grade 50 microalloyed steels submerged arc welded with Linde 40B weld metal to determine the fracture properties of base plates, weld metal and heat-affected zones. The effects of plate orientation, heat treatment, heat input, and postweld heat treatments on heat-affected zone toughness were included in the investigation.

Effects of Long-Time Postweld Heat Treatment on the Properties of Constructional-Steel Weldments
By P. J. Konkol

To aid steel users in the selection of steel grades and fabrication procedures for structures subject to PWHT, seven representative carbon and high-strength low-alloy plate steels were welded by shielded metal arc welding and by submerged arc welding. The weldments were PWHT for various times up to 100 h at 1100°F (593°C) and 1200°F (649°C). The mechanical properties of the weldments were determined by means of base-metal tension tests, transverse-weld tension tests, HAZ hardness tests, and Charpy V-notch (CVN) impact tests of the base metal, HAZ and weld metal.

Publication of these reports was sponsored by the Subcommittee on Thermal and Mechanical Effects on Materials of the Welding Research Council. The price of WRC Bulletin 330 is $20.00 per copy, plus $5.00 for postage and handling. Orders should be sent with payment to the Welding Research Council, 345 E. 47th St., Suite 1301, New York, NY 10017.

WRC Bulletin 337
October 1988

Experimental Validation of the Evaluation of Reinforced Openings in Large Steel Pressure Vessels
By J. Schroeder

Experimental techniques and test results of a large, very thin pressure vessel loaded on a very small nozzle are reported. The results indicate that analytical results can overestimate nondimensional stress resultants. Stress resultants of large, very thin vessels appear to be independent of the nozzle thickness, when the thickness of the vessel is not much larger or smaller than that of the nozzle.

Publication of this report was sponsored by the Subcommittee on Reinforced Openings and External Loadings of the Pressure Vessel Research Committee of the Welding Research Council. The price of WRC Bulletin 337 is $20.00 per copy, plus $5.00 for postage and handling. Orders should be sent with payment to the Welding Research Council, 345 E. 47th St., Suite 1301, New York, NY 10017.